Helicity sensitive enhancement of strong-field ionization in circularly polarized laser fields

Xiaosong Zhu,[1] Pengfei Lan,[1] Kunlong Liu,[2] Yang Li,[1] Xi Liu,[1] Qingbin Zhang,[1] Ingo Barth,[2,4] and Peixiang Lu[1,3⋆]

[1] *Wuhan National Laboratory for Optoelectronics and School of Physics, Huazhong University of Science and Technology, Wuhan 430074, China*
[2] *Max Planck Institute of Microstructure Physics, 06120 Halle (Saale), Germany*
[3] *Laboratory of Optical Information Technology, Wuhan Institute of Technology, Wuhan 430205, China*
[4] *barth@mpi-halle.mpg.de*
[⋆] *lupeixiang@mail.hust.edu.cn*

Abstract: We investigate the strong-field ionization from $p_{\pm}$ orbitals driven by circularly polarized laser fields by solving the two-dimensional time-dependent Schrödinger equation in polar coordinates with the Lagrange mesh technique. Enhancement of ionization is found in the deep multiphoton ionization regime when the helicity of the laser field is opposite to that of the p electron, while this enhancement is suppressed when the helicities are the same. It is found that the enhancement of ionization is attributed to the multiphoton resonant excitation. The helicity sensitivity of the resonant enhancement is related to the different excitation-ionization channels in left and right circularly polarized laser fields.

OCIS codes: (020.4180) Multiphoton process; (260.3230) Ionization.

References and links

1. D. B. Milošević, G. G. Paulus, D. Bauer, and W. Becker, "Above-threshold ionization by few-cycle pulses," J. Phys. B: At. Mol. Opt. Phys. **39,** R203–R262 (2006).
2. W. Becker, F. Grasbon, R. Kopold, D. B. Milošević, G.G. Paulus, and H. Walther, "Above-threshold ionization: from classical features to quantum effects," Adv. At. Mol. Opt. Phys. **48,** 35–98 (2002).
3. D. B. Milošević and F. Ehlotzky, "Scattering and reaction processes in powerful laser fields," Adv. At. Mol. Opt. Phys. **49,** 373–532 (2003).
4. A. Becker and F. H. M. Faisal, "Intense-field many-body S-matrix theory," J. Phys. B: At. Mol. Opt. Phys. **38,** R1–R56 (2005).
5. B. Walker, B. Sheehy, L. F. DiMauro, P. Agostini, K. J. Schafer, and K. C. Kulander, "Precision measurement of strong field double ionization of helium," Phys. Rev. Lett. **73,** 1227 (1994).
6. R. Moshammer, B. Feuerstein, W. Schmitt, A. Dorn, C. D. Schröter, J. Ullrich, H. Rottke, C. Trump, M. Wittmann, G. Korn, K. Hoffmann, and W. Sandner, "Momentum distributions of Ne^{n+} ions created by an intense ultrashort laser pulse," Phys. Rev. Lett. **84,** 447–450 (2000).
7. C. F. M. Faria and X. Liu, "Electron-electron correlation in strong laser fields," J. Mod. Opt. **58,** 1076–1131 (2011).
8. Y. Zhou, C. Huang, Q. Liao, and P. Lu, "Classical simulations including electron correlations for sequential double ionization," Phys. Rev. Lett. **109,** 053004 (2012).
9. Y. Mairesse, A. de Bohan, L. J. Frasinski, H. Merdji, L. C. Dinu, P. Monchicourt, P. Breger, M. Kovačev, R. Taïzeb, B. Carré, H. G. Muller, P. Agostini, and P. Salères, "Attosecond synchronization of high-harmonic soft X-rays," Science **302,** 1540–1543 (2003).

#257645 Received 20 Jan 2016; revised 15 Feb 2016; accepted 16 Feb 2016; published 19 Feb 2016

10. E. Goulielmakis, M. Schultze, M. Hofstetter, V. S. Yakovlev, J. Gagnon, M. Uiberacker, A. L. Aquila, E. M. Gullikson, D. T. Attwood, R. Kienberger, F. Krausz, U. Kleineberg, "Single-cycle nonlinear optics," Science **320,** 1614–1617 (2008).
11. O. Smirnova, Y. Mairesse, S. Patchkovskii, N. Dudovich, D. Villeneuve, P. Corkum, and M. Y. Ivanov, "High harmonic interferometry of multi-electron dynamics in molecules," Nature **460,** 972–977 (2009).
12. X.-B. Bian, and A. D. Bandrauk, "Probing nuclear motion by frequency modulation of molecular high-order harmonic generation," Phys. Rev. Lett. **113,** 193901 (2014).
13. L. He, P. Lan, Q. Zhang, C. Zhai, F. Wang, W. Shi, and P. Lu, "Spectrally resolved spatiotemporal features of quantum paths in high-order-harmonic generation," Phys. Rev. A **92,** 043403 (2015).
14. F. Wang, L. He, C. Zhai, W. Shi, Q. Zhang, P. Lan, and P. Lu, "Time-dependent phase matching of high-order-harmonic generation," Phys. Rev. A **92,** 063839 (2015).
15. P. Eckle, M. Smorlarski, P. Schlup, J. Biegert, A. Staudte, M. Schöffler, H. G. Muller, R. Dörner, and U. Keller, "Attosecond angular streaking," Nat. Phys. **4,** 565–570 (2008).
16. P. Eckle, A. N. Pfeiffer, C. Cirelli, A. Staudte, R. Dörner, H. G. Muller, M. Bütticker, and U. Keller, "Attosecond ionization and tunneling delay time measurements in helium," Science **322,** 1525–1529 (2008).
17. A. N. Pfeiffer, C. Cirelli, M. Smorlarski, D. Dimitrovski, M. Abu-samha, L. B. Madsen, and U. Keller, "Attoclock reveals natural coordinates of the laser-induced tunnelling current flow in atoms," Nat. Phys. **8,** 76–80 (2012).
18. J. Wu, M. Meckel, L. P. Schmidt, M. Kunitski, S. Voss, H. Sann, H. Kim, T. Jahnke, A. Czasch, and R. Dörner, "Probing the tunnelling site of electrons in strong field enhanced ionization of molecules," Nat. Commun. **3,** 1113 (2012).
19. J. Wu, L. Schmidt, M. Kunitski, M. Meckel, S. Voss, H. Sann, H. Kim, T. Jahnke, A. Czasch, and R. Dörner, "Multiorbital tunneling ionization of the CO molecule," Phys. Rev. Lett. **108,** 183001 (2012).
20. L. Holmegaard, J. L. Hansen, L. Kalhøj, S. L. Kragh, H. Stapelfeldt, F. Filsinger, J. Küpper, G. Meijer, D. Dimitrovski, M. Abu-samha, C. P. J. Martiny, and L. B. Madsen, "Photoelectron angular distributions from strong-field ionization of oriented molecules," Nat. Phys. **6,** 428–432 (2010).
21. J. Hansen, H. Stapelfeldt, D. Dimitrovski, M. Abu-samha, C. Martiny, and L. Madsen, "Time-resolved photo-electron angular distributions from strong-field ionization of rotating naphthalene molecules," Phys. Rev. Lett. **106,** 073001 (2011).
22. X. Zhu, Q. Zhang, W. Hong, P. Lu, and Z. Xu, "Molecular orbital imaging via above-threshold ionization with circularly polarized pulses," Opt. Express **19,** 13722–13731 (2011).
23. I. Petersen, J. Henkel, and M. Lein, "Signatures of molecular orbital structure in lateral electron momentum distributions from strong-field ionization," Phys. Rev. Lett. **114,** 103004 (2015).
24. G. Yudin, and M. Ivanov, "Nonadiabatic tunnel ionization: looking inside a laser cycle," Phys. Rev. A **64,** 013409 (2001).
25. M. V. Ammosov, N. B. Delone, and V. P. Krainov, "Tunnel ionization of complex atoms and of atomic ions in an alternating electrom," Sov. Phys. JETP **64,** 1191 (1986).
26. X. M. Tong, Z. X. Zhao, and C. D. Lin, "Theory of molecular tunneling ionization," Phys. Rev. A **66,** 033402 (2002).
27. I. Barth, and O. Smirnova, "Nonadiabatic tunneling in circularly polarized laser fields: physical picture and calculations," Phys. Rev. A **84,** 063415 (2011);
28. I. Barth, and O. Smirnova, "Nonadiabatic tunneling in circularly polarized laser fields. II. Derivation of formulas," Phys. Rev. A **87,** 013433 (2013).
29. I. Barth, and M. Lein, "Numerical verification of the theory of nonadiabatic tunnel ionization in strong circularly polarized laser fields," J. Phys. B: At. Mol. Opt. Phys. **47**, 204016 (2014).
30. T. Herath, L. Yan, S. K. Lee, and W. Li, "Strong-field ionization rate depends on the sign of the magnetic quantum number," Phys. Rev. Lett. **109,** 043004 (2012).
31. Y. Li, P. Lan, H. Xie, M. He, X. Zhu, Q. Zhang, and P. Lu, "Nonadiabatic tunnel ionization in strong circularly polarized laser fields: counterintuitive angular shifts in the photoelectron momentum distribution," Opt. Express **23,** 28801–28807 (2015).
32. J. Kaushal, F. Morales, and O. Smirnova, "Opportunities for detecting ring currents using an attoclock setup," Phys. Rev. A **92,** 063405 (2015).
33. I. Barth, and O. Smirnova, "Spin-polarized electrons produced by strong-field ionization," Phys. Rev. A **88,** 013401 (2013).
34. A. D. Bandrauk, and Huizhong Lu, *High Performance Computing Systems and Applications* (Springer, 2010), Chapter 8.
35. C. Lefebvre, Huizhong Lu, and A. D. Bandrauk, "Numerical method for dynamic imaging of nonlinear poly-atomic molecules," J. Phys. Coference Series **341**, 012004 (2012).
36. M. Vincke, L. Malegat, and D. Baye, "Regularization of singularities in Lagrange-mesh calculations," J. Phys. B: At. Mol. Opt. Phys. **26**, 811–826 (1993).
37. D. Baye, L. Filippin, and M. Godefroid, "Accurate solution of the Dirac equation on Lagrange meshes," Phys. Rev. E **89**, 043305(2014).
38. D. Dundas, "Accurate and efficient non-adiabatic quantum molecular dynamics approach for laser-matter inter-

#257645 Received 20 Jan 2016; revised 15 Feb 2016; accepted 16 Feb 2016; published 19 Feb 2016

actions," J. Phys. B: At. Mol. Opt. Phys. **37**, 2883–2901 (2004).
39. L. Y. Peng, J. F. McCann, D. Dundas, K. T. Taylor, and I. D. Williams, "A discrete time-dependent method for metastable atoms and molecules in intense fields," J. Chem. Phys. **120**, 10046 (2004).
40. M. Abramowitz, and I. A. Stegun, *Handbook of Mathematical Functions* (Dover Publications, 1965).
41. M. D. Perry, A. Szoke, and K. C. Kulander, "Resonantly enhanced above-threshold ionization of helium," Phys. Rev. Lett. **63,** 1058–1061 (1989).
42. M. Li, P. Zhang, S. Luo, Y. Zhou, Q. Zhang, P. Lan, and P. Lu, "Selective enhancement of resonant multiphoton ionization with strong laser fields," Phys. Rev. A **92,** 063404 (2015).
43. K. Liu, Q. Li, P. Lan, and P. Lu, "Enhanced dissociation of H^{2+} into highly excited states by UV pulses," Molecular Physics **21,** 3247–3252 (2015).

1. Introduction

Strong-field ionization is the first step of consequent strong-field processes such as high-order above-threshold ionization [1–4], nonsequential/sequential double ionization [5–8] and high-order harmonic generation [9–14]. Therefore, investigation on the strong-field ionization is of great importance for the research area of strong-field physics. On the other hand, manipulation of the strong-field ionization process itself stimulates many applications such as attosecond angular streaking [15–19] and molecular orbital probing [20–23], which help people gain a deeper insight into the microscopic (Ångstrom scale) and ultrafast (attosecond scale) world. The strong-field ionization process can be understood in the multiphoton or tunneling regime determined by the Keldysh parameter $\gamma = \omega_0\sqrt{2I_p}/E_0$ (I_p is the ionization potential of the target, E_0 and ω are the peak amplitude and frequency of the laser field, respectively, atomic units are used through this paper). $\gamma \ll 1$ indicates the ionization is dominated by tunneling and $\gamma \gg 1$ indicates the ionization is better understood as multiphoton ionization. $\gamma \approx 1$ is the grey area between two regimes usually viewed as the non-adiabatic tunneling regime [16, 24]. The ionization process in both regimes has been widely investigated in the past tens of years.

Previously, it was generally considered that the strong-field ionization rate is only related to the modulus of magnetic quantum number $|m|$ of the target orbital [24–26]. However, it was recently shown that the ionization rate under circularly polarized laser field is also dependent on the sign of non-zero m (i.e. the direction of angular momentum of the "orbiting" electron) both in theory [27, 28] and numerical simulations [29]. Specifically, the strong field preferentially removes the electron counter-rotating to the circularly polarized laser field rather than the co-rotating electron. This predication has been partially proved in experiment by measuring strong-field sequential double ionization yields of argon in two time-delayed near-circularly polarized laser pulses with same and opposite helicities [30]. Studies on the strong-field ionization from states with non-zero angular momentum also suggest new applications. For example, it was found that the internal angular momentum will shift the offset angle of the maximum in the photoelectron momentum distribution in an angular streaking setup, which offers a potential tool for studying orbital structures and ring currents in atomic and molecular systems [31, 32]. It was also proposed to produce photoelectrons with up to 100% spin polarization resulting from m-dependent strong-field ionization and spin-orbit coupling [33].

In this work, strong-field ionization of $p_\pm$ orbitals under circularly polarized laser fields in the wide range of wavelengths from deep multiphoton regime to tunneling regime is investigated. The ionization processes are simulated by numerically solving the two-dimensional time-dependent Schrödinger equation (2D-TDSE) in polar coordinates with the Lagrange mesh technique. Ionization peaks are observed in the deep multiphoton ionization regime when the electric field counter-rotates to the p electron, while the peaks vanish when the electric field co-rotates with the p electron. It is shown that these peaks result from the resonant enhancement of ionization and the helicity sensitivity is due to different excitation-ionization channels.

#257645 Received 20 Jan 2016; revised 15 Feb 2016; accepted 16 Feb 2016; published 19 Feb 2016

2. Theoretical model

In this section, we present an efficient and accurate method for the non-perturbative numerical solution of the 2D-TDSE in polar coordinates. To simulate the ionization dynamics of a valence p electron in a strong circularly polarized laser pulse, we consider to solve the 2D-TDSE

$$\begin{aligned} i\frac{\partial\Psi(\mathbf{r},t)}{\partial t} &= \left[-\frac{\nabla^2}{2}+V_c(r)+V_e(\mathbf{r},t)\right]\Psi(\mathbf{r},t) \\ &= \left[-\frac{1}{2}\left(\frac{1}{\rho}\frac{\partial}{\partial\rho}\rho\frac{\partial}{\partial\rho}+\frac{1}{\rho^2}\frac{\partial^2}{\partial\theta^2}\right)+V_c(\rho)+\mathbf{r}\cdot\mathbf{E}_{\pm}(t)\right]\Psi(\mathbf{r},t), \end{aligned} \tag{1}$$

in polar coordinates, where $\mathbf{r}=\rho\cos\theta\,\mathbf{e}_x+\rho\sin\theta\,\mathbf{e}_y$. The right (+) and left (−) circularly polarized electric field $\mathbf{E}_{\pm}(t)$ is expressed by

$$\mathbf{E}_{\pm}(t)=E_0\sin^2\left(\frac{t\pi}{\tau}\right)[\cos(\omega_0 t)\mathbf{e}_x\pm\sin(\omega_0 t)\mathbf{e}_y] \tag{2}$$

where E_0 is the amplitude, ω_0 is the angular frequency, τ is the total duration of the laser pulse and $0\le t\le\tau$. Therefore, $V_e(\mathbf{r},t)=\rho\cos\theta\,E_0\sin^2(t\pi/\tau)\cos(\omega_0 t)+\rho\sin\theta\,E_0\sin^2(t\pi/\tau)\sin(\omega_0 t)$. As in [29], we consider a 2D model of neon atom and the effective Coulomb potential $V_c(\rho)$ is written as

$$V_c(\rho)=-\frac{Z_c}{\sqrt{\rho^2+a}}=-\frac{1+9\exp(-\rho^2)}{\sqrt{\rho^2+a}} \tag{3}$$

with the soft-core parameter $a=2.88172$, that enables us to obtain the correct energy of the valence 2p orbital of -0.793 a.u. [29].

The numerical difficulty in Eq. (1) comes from the singularity of the Laplacian in polar coordinates. To overcome this difficulty, Bandrauk *et al.* [34,35] introduced a unitary discrete Laplacian operator and adopted the Crank-Nicholson method to solve Eq. (1). However, this method does not insure that the wave function $\Psi(\mathbf{r},t)=\Psi(\rho,\theta,t)$ can completely eliminate the parasite modes. Note that a function contains parasite modes is not a regular function and can lead to error and unstabitily in the simulation. To minimize this error, a more general Crank-Nicholson scheme has to be used in [34, 35]. On the other hand, special carefulness should be paid to the problem of singularity at the boundary $\rho=0$. In this work, we introduce a more efficient and accurate way to solve Eq. (1) by adopting the Lagrange mesh technique [36]. The effectiveness of the Lagrange mesh method has been demonstrated in lots of applications [37–39], e.g. solutions of Dirac equations [37], time-dependent Kohn-Sham equations [38], and also TDSE in spheroidal [36] and cylindrical coordinates [39]. Here, we solve Eq. (1) by utilizing the Lagrange mesh method for polar coordinates. Details about the Lagrange mesh technique are summarized in [36]. In the following, we outline our method in solving TDSE.

First, we remove the first derivative in ρ by introducing the new wave function

$$\psi(\rho,\theta,t)=\frac{1}{\sqrt{\rho}}\Psi(\rho,\theta,t). \tag{4}$$

Then, the TDSE (1) becomes

$$i\frac{\partial\psi(\rho,\theta,t)}{\partial t}=\left[-\frac{1}{2}\left(\frac{\partial^2}{\partial\rho^2}+\frac{1}{4\rho^2}+\frac{1}{\rho^2}\frac{\partial^2}{\partial\theta^2}\right)+V_c(\rho)+\mathbf{r}\cdot\mathbf{E}_{\pm}(t)\right]\psi(\rho,\theta,t). \tag{5}$$

Second, the wave function is discretized in polar coordinates. The numbers of discrete points for ρ and θ are defined as N and M, respectively. It follows that the maximum possible numbers

#257645 Received 20 Jan 2016; revised 15 Feb 2016; accepted 16 Feb 2016; published 19 Feb 2016

of basis functions in ρ and θ are N and M, respectively. For the discretization of θ, we use the truncated Fourier series

$$\psi(\rho,\theta,t) = \frac{1}{M}\sum_{m=-M/2}^{M/2-1} \phi_m(\rho,t)\exp(im\theta), \tag{6}$$

which can be effectively calculated by using the discrete fast Fourier transform algorithm. By inserting Eq. (6) into Eq. (5), we get

$$\begin{aligned} i\frac{\partial \phi_m(\rho,t)}{\partial t} &= [T_\rho + T_\theta + V_c(\rho) + \mathbf{r}\cdot\mathbf{E}_\pm(t)]\phi_m(\rho,t) \\ &= \left[-\frac{1}{2}\left(\frac{\partial^2}{\partial\rho^2}+\frac{1}{4\rho^2}\right)+\frac{m^2}{2\rho^2}+V_c(\rho)+\mathbf{r}\cdot\mathbf{E}_\pm(t)\right]\phi_m(\rho,t). \end{aligned} \tag{7}$$

Next, we consider to treat the coordinate ρ with the Lagrange mesh method. As in [36,39], we rescale the radial variable $\rho = hx$, where the scaling factor h is set to be 0.065 in our simulation. The mesh points x_i are the roots of $L_N^\alpha(x_i) = 0$, where $i = 1,\ldots,N$ and L_N^α is the generalized Laguerre polynomial [40]. Note that such mesh points are nonuniformly spaced: Very dense grid points are located at the origin and, therefore, the Coulomb potential can be accurately described. On the other hand, the grid points becomes more and more sparse as ρ increases, where the Coulomb potential becomes weak and smooth. Note that uniform grid points are commonly adopted in the finite difference method [34, 35]. In this case, a large number of grid points are required to accurately represent the Coulomb potential because of the singularity at the origin. By contrast, the Lagrange mesh is more efficient and requires less grid points than the uniform grid mesh. Then, we consider to reconstruct a set of orthonormal basis functions based on the generalized Laguerre polynomials [36]

$$g_n(x) = \left(\frac{\Gamma(n+1)}{\Gamma(\alpha+n+1)}\right)^{1/2} x^{\alpha/2}e^{-x/2}L_n^\alpha(x), \tag{8}$$

where $n = 1,\ldots,N$. These functions form an orthonormal set in the range [0, ∞),

$$\int_0^\infty g_l(x)g_n(x) = \delta_{ln}. \tag{9}$$

The corresponding Lagrange functions can be constructed by

$$f_i(x) = \lambda_i^{-1/2}\left(\frac{1}{g_N'(x_i)}\right)\frac{g_N(x)}{x-x_i}, \tag{10}$$

where x_i are the Lagrange mesh points and

$$\lambda_i = \frac{1}{x_i g_N'(x_i)^2}. \tag{11}$$

These functions are discrete, orthonormal, and also obey the Lagrange interpolation formula. By adopting the Gaussian quadrature, we get matrix elements for the Hamiltonian with the basis functions obtained from Eq. (10) as

$$(T_\rho)_{ij} = \frac{1}{2h^2}\times\begin{cases} \frac{(\alpha+1)^2}{4x_i^2}+S_{ii}, & (i=j) \\ (-1)^{i-j}\left[\frac{\alpha+1}{2\sqrt{x_i x_j}}\left(\frac{1}{x_i}+\frac{1}{x_j}\right)+S_{ij}\right] & (i\neq j), \end{cases}$$

#257645 Received 20 Jan 2016; revised 15 Feb 2016; accepted 16 Feb 2016; published 19 Feb 2016

where

$$S_{ij} = \sqrt{x_i x_j} \sum_{p \neq i,j} \frac{1}{x_p(x_p - x_j)(x_p - x_i)}. \tag{12}$$

Note that, in our calculation, the generalized Laguerre polynomial L_N^{α} with $\alpha = 1$ is applied. More details can be found in [36]. Moreover, one can easily derive that

$$(T_\theta)_{ij} = \frac{m^2}{2h^2 x_i^2} \delta_{ij} \tag{13}$$

and

$$(V_c)_{ij} = -\frac{Z_c}{\sqrt{h^2 x_i^2 + a}} \delta_{ij}. \tag{14}$$

We apply the second-order split-operator method to solve the propagation of the wave function in time

$$\psi(\rho,\theta,t+\delta t) = \exp(-iH_0\delta t/2)\exp(-iV_e\delta t)\exp(-iH_0\delta t/2)\psi(\rho,\theta,t) + O(\delta t^3), \tag{15}$$

where H_0 is the field-free Hamiltonian. The propagation can be split into three steps. The first step is

$$\begin{aligned} \psi^{(1)}(\rho,\theta,t) &= \exp(-iH_0\delta t/2)\psi(\rho,\theta,t) \\ &= \frac{1}{M}\sum_{m=-M/2}^{M/2-1} \exp(im\theta)\exp[-iH_0^{(m)}\delta t/2]\phi_m(\rho,t), \end{aligned} \tag{16}$$

where $H_0^{(m)} = T_\rho + T_\theta + V_c$. The propagator $\exp[-iH_0^{(m)}\delta t/2]$ can be built by eigenvectors $\chi_k^{(m)}$ and eigenvalues $\eta_k^{(m)}$ of the field-free Hamiltonian

$$\exp[-iH_0^{(m)}\delta t/2] = \sum_{k=1}^{N} \exp(-i\eta_k^{(m)}\delta t/2) \times |\chi_k^{(m)}\rangle\langle\chi_k^{(m)}|. \tag{17}$$

Note that the field-free m-dependent Hamiltonian $H_0^{(m)}$ is a $N \times N$ matrix and its elements are expressed by Eqs. (12)–(14). Since the Hamiltonian $H_0^{(m)}$ depends on the value of m^2, we need to solve $M/2$ eigenvalue equations $H_0^{(m)}\chi_k^{(m)} = \eta_k^{(m)}\chi_k^{(m)}$.

The external field operator $\exp(-iV_e\delta t)$ is a diagonal matrix in coordinate representation. Therefore, the second step of the short-time propagation can be multiplied straightforwardly

$$\psi^{(2)}(\rho,\theta,t) = \exp(-iV_e\delta t) \times \psi^{(1)}(\rho,\theta,t). \tag{18}$$

Then, $\psi^{(2)}(\rho,\theta,t)$ is expanded in the Fourier series again and the third step of the short-time propagation is treated as the same as the first step,

$$\begin{aligned} \psi^{(3)}(\rho,\theta,t) &= \exp(-iH_0\delta t/2)\psi^{(2)}(\rho,\theta,t) \\ &= \frac{1}{M}\sum_{m=-M/2}^{M/2-1} \exp(im\theta)\exp[-iH_0^{(m)}\delta t/2]\phi_m^{(2)}(\rho,t). \end{aligned} \tag{19}$$

This procedure completes the short-time propagation according to Eq. (15), i.e. $\psi(\rho,\theta,t+\delta t) = \psi^{(3)}(\rho,\theta,t)$. By repeating this process, the wave function can be obtained sequentially

#257645 Received 20 Jan 2016; revised 15 Feb 2016; accepted 16 Feb 2016; published 19 Feb 2016

starting at $t = 0$ and ending at $t = \tau$. The initial state is adopted by the eigenvector corresponding to the 2p orbital and the ionization energy (i.e. the negative eigenvalue of the field-free Hamiltonian) is 0.793 a.u.. Note that there are two degenerate 2p orbitals: the one with magnetic quantum number $m = -1$ is $2p_-$ and the one with $m = 1$ is $2p_+$.

To avoid unphysical reflections at grid boundaries and to calculate ionization yields, the wave function $\psi^{(3)}(\rho,\theta,t)$ in our simulation is multiplied by an absorbing function

$$W(\rho) = \begin{cases} 1, & (\rho \le \rho_{abs}) \\ \sin^2\left[\frac{(\rho_{max}-\rho)\pi}{2(\rho_{max}-\rho_{abs})}\right] & (\rho > \rho_{abs}). \end{cases}$$

Without absorbing function, the norm of the time-dependent wave function is kept to be 1. However, with absorbing function, the norm decays with the increase of t and the time-dependent depletion of the initial wavefunction can be calculated as

$$P_1(t) = 1 - |\psi(\rho,\theta,t)|^2. \tag{20}$$

On the other hand, since the eigenvalue equations of the field-free Hamiltonian are solved in our simulation, we can also calculate the time-dependent population in the continuum as

$$P_2(t) = 1 - \sum_{m=1}^{M} \sum_{\substack{k=1 \\ \eta_k^{(m)}<0}}^{N} |\langle \chi_k^{(m)} | \psi(\rho,\theta,t)\rangle|^2. \tag{21}$$

The ionization probability can be determined from P_1 and P_2 at the end of the laser pulse.

To test the above Lagrange mesh scheme, we simulate the ionization process in a few-cycle laser pulse. As in [29], the pulse duration is set to be 3 optical cycles, the electric field amplitude is 0.09 a.u., and the wavelength is 800 nm. The grid mesh has $N \times M = 900 \times 90$ points. In this case, the maximum of ρ is $\rho_{max} \approx 230$ a.u., which is twice of that in [29], and ρ_{abs} is set to be 60 a.u.. By contrast, large grid points of 2048×2048 are needed in [29]. As discussed above, the nonuniform grid used in Lagrange mesh scheme is much more efficient. Furthermore, since the short-time propagator is built by eigenvectors and eigenvalues, the simulation procedure is quite stable and the results converge already at $\delta t = 0.1$ a.u.. By contrast, a much smaller time step of $\delta t = 0.005$ a.u. is adopted in [29]. Therefore, the computation time can be greatly shortened by using our method. Figure 1 shows the calculated $P_1(t)$ and $P_2(t)$ by using a right circularly polarized laser field. It is found that the ionization probabilities and the ratios of the ionization rates from $2p_-$ to $2p_+$ orbitals agree well with those in [29]. We also calculate the ionization ratios for other laser parameters listed in Table I of [29] and the values of ratios agree with those in [29] to the first decimal places.

3. Result and discussion

Below, we investigate the ionization probability in a wide range of laser wavelengths. Throughout the following simulations, the laser pulse is sine squared with total pulse duration of 10 optical cycles. We scan the laser wavelength in the range from 110 nm to 6400 nm for laser intensities 5×10^{14} W/cm^2 and 1×10^{15} W/cm^2. Both right and left circularly polarized laser fields are considered. For right circularly polarized laser fields, the $2p_-$ electron is counter-rotating with respect to the rotation of the laser field and the $2p_+$ electron is co-rotating. For left circularly polarized laser fields, the $2p_-$ electron is co-rotating and the $2p_+$ electron is counter-rotating.

The ionization probabilities for the $2p_-$ orbital are shown in Fig. 2 as blue (for $I = 5 \times 10^{14}$ W/cm^2) and red (for $I = 1 \times 10^{15}$ W/cm^2) curves. Results with right circularly polarized laser

#257645 Received 20 Jan 2016; revised 15 Feb 2016; accepted 16 Feb 2016; published 19 Feb 2016

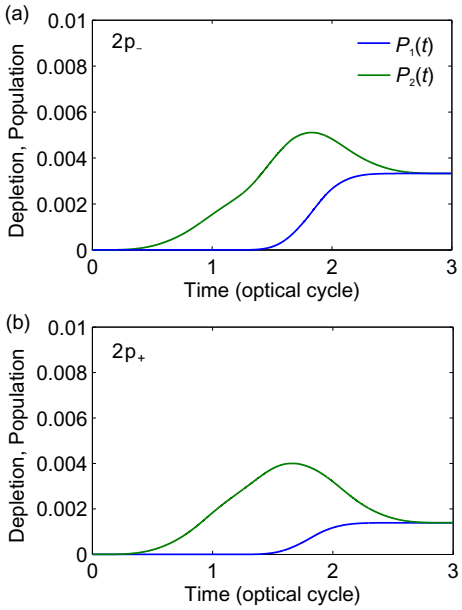

Fig. 1. Time-dependent depletions of the initial wavefunctions $P_1(t)$ and time-dependent populations in the continuum $P_2(t)$ for (a) $2p_-$ and (b) $2p_+$ orbitals driven by a right circularly polarized 3-cycle laser field with 800 nm and $E_0 = 0.09$ a.u.

fields are presented as solid curves and results with left circularly polarized laser fields are presented as dashed curves. Three phenomena are found in Fig. 2. First, in all cases, the ionization probability drops rapidly when the short wavelength increases. Then, it stays approximately the same forming a minimum and finally increases gradually with the increase of the laser wavelength. To better understand the variation of the ionization probability, we calculate Keldysh parameters γ for different laser parameters.

The values of γ for the minima of four curves are approximately in the range from 0.4 to 1 as shown in Fig. 2. Therefore, the tendency of the ionization probabilities can be understood. For short wavelengths before the minima, the orbital is ionized via multiphoton ionization. With the increase of the laser wavelength, the necessary number of photons for ionization increases, leading to the dramatic decrease of the ionization rate. Then, with the further increasing of the laser wavelength, the ionization regime changes into the tunneling regime. In this case, the ionization rate is not sensitive to the wavelength and the decrease of the ionization rate slows down. On the other side, the laser pulse duration increases with the increase of the laser wavelength (the pulse duration is 10 optical cycles for different wavelengths) and it finally leads to the increase of the ionization probability.

The second phenomenon in Fig. 2 is that, in the short wavelength region, the ionization probabilities for right circularly polarized laser fields (counter-rotating to the $2p_-$ electron) are larger than those for left circularly polarized laser fields (co-rotating with the $2p_-$ electron) as indicated in [27–29]. In the very long wavelength region, the ionization probabilities for right circularly laser fields are smaller than those for left circularly polarized laser fields. This phenomenon was also found in numerical simulations in [29] and is due to the role of the adiabatic laser-dressed orbitals. The Keldysh parameters at the cross points of the solid and dashed curves are also shown in Fig. 2. The values at the cross points are about 0.2, which agree with those in [29].

#257645 Received 20 Jan 2016; revised 15 Feb 2016; accepted 16 Feb 2016; published 19 Feb 2016

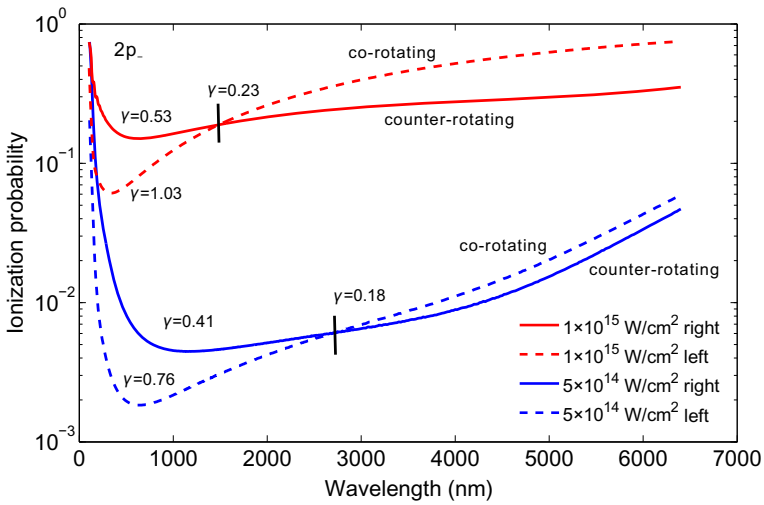

Fig. 2. Ionization probabilities for the $2p_-$ orbital and for laser intensities $I = 5 \times 10^{14}$ W/cm^2 (blue curve) and $I = 1 \times 10^{15}$ W/cm^2 (red curve) and laser wavelengths varying from 110 nm to 6400 nm. Results for right circularly polarized laser fields are presented as solid curves and results for left circularly polarized laser fields are presented as dashed curves.

The third phenomenon is the oscillation in the very short wavelength region for right circularly polarized intense ($I = 1 \times 10^{15}$ W/cm^2) laser fields, which can be more clearly observed in Fig. 3. In Fig. 3, we zoom into the range from 110 nm to 300 nm and calculate the ionization probabilities for laser intensities from $I = 1.1 \times 10^{15}$ W/cm^2 to 1.5×10^{15} W/cm^2. The results for the $2p_-$ orbital are shown in Fig. 3(a) and those for the $2p_+$ orbital are shown in Fig. 3(b). The ionization probabilities for right circularly polarized laser fields are presented as solid curves and those for left circularly polarized laser fields are presented as dashed curves. It shows that the ionization peaks indicating enhancement of ionization appear only in solid curves of Fig. 3(a) and in dashed curves of Fig. 3(b). The first peak at the short wavelength side is strongest and the subsequent peaks become weaker and finally disappear. At first sight, it seems that the peaks appear for high ionization probabilities. To check whether the appearance of the peaks is determined by the ionization probability, we also calculate the ionization probabilities for much higher intensities $I = 2.0 \times 10^{15}$ W/cm^2 and $I = 3.0 \times 10^{15}$ W/cm^2 for the $2p_-$ orbital under left circularly polarized laser field. The corresponding results are shown as additional dotted curves in Fig. 3(a): Although the ionization probabilities are already very high, the peaks are still not found. Therefore, we conclude that the appearance of the peaks is not related to high ionization probabilities.

The above results and discussion indicate that the appearance of the peaks is associated with the relative helicity between the electric field and the p electron. The ionization enhancement occurs at particular laser wavelengths when the electric field rotates in the opposite direction of the p electron (i.e. the sign of the spin of the photon and the sign of the angular momentum of the p orbital are different). The ionization enhancement is suppressed when the electric field and p electron rotate in the same direction (i.e. the sign of the spin of the photon and the sign of the angular momentum of the p orbital are the same). Note that, with the increase of the laser intensity, the positions of the peaks shift to shorter wavelengths.

As a comparison, Fig. 4 shows the ionization probabilities for $2p_\pm$ orbitals driven by linearly polarized laser fields with laser intensities from $I = 1.1 \times 10^{15}$ W/cm^2 to 1.5×10^{15} W/cm^2.

#257645 Received 20 Jan 2016; revised 15 Feb 2016; accepted 16 Feb 2016; published 19 Feb 2016

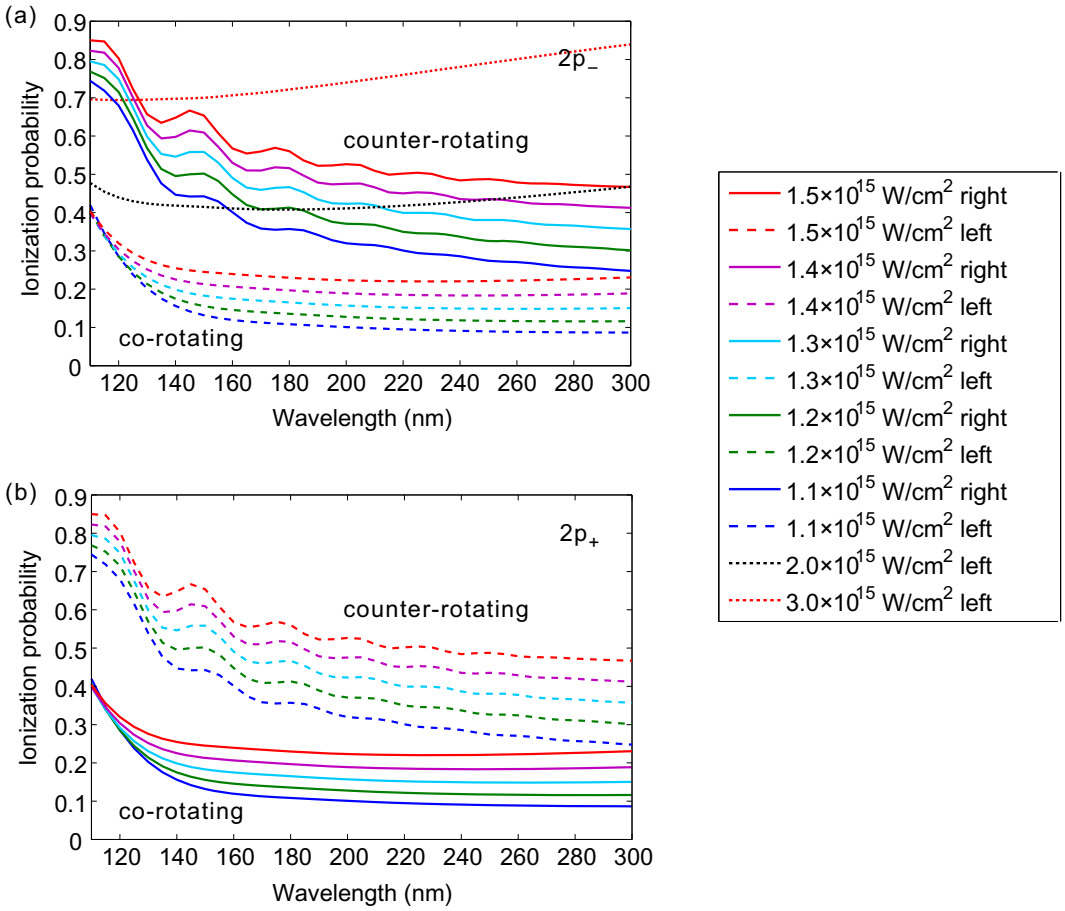

Fig. 3. Ionization probabilities for (a) $2p_-$ and (b) $2p_+$ orbitals and for laser intensities from $I = 1.1 \times 10^{15}$ W/cm^2 to 1.5×10^{15} W/cm^2 and laser wavelengths varying from 110 nm to 300 nm. Ionization probabilities for the $2p_-$ orbital and for much higher intensities $I = 2.0 \times 10^{15}$ W/cm^2 and $I = 3.0 \times 10^{15}$ W/cm^2 of the left circularly polarized laser field are also shown as additional dotted curves in panel (a).

This figure shows that the ionization peaks appear for both $2p_-$ and $2p_+$ orbitals and the corresponding curves of the ionization probability are the same for each laser intensity. Similarly, with the increase of the laser intensity, the positions of the peaks shift to shorter wavelength. These results show that the ionization enhancement also exists for linearly polarized driving laser fields, while the enhancement is insensitive to the rotation direction of the p electron.

The wavelength dependent ionization enhancement can be understood as the resonant enhancement [41–43], where the electron is first resonantly promoted to the excited state via resonant multiphoton excitation and then removed from this excited state. With the increase of the laser intensity, the photon density increases and the probability of the multiphoton excitation becomes larger. Therefore, the enhancement peaks appear when the laser intensity is high. With the increase of the laser intensity, the positions of the peaks shift to shorter wavelengths because the energy gaps between the ground and excited states are enlarged due to the Stark effect. The remaining question why the enhancement is sensitive to the relative helicity between the circularly polarized laser field and the p orbital will be answered below.

#257645 Received 20 Jan 2016; revised 15 Feb 2016; accepted 16 Feb 2016; published 19 Feb 2016

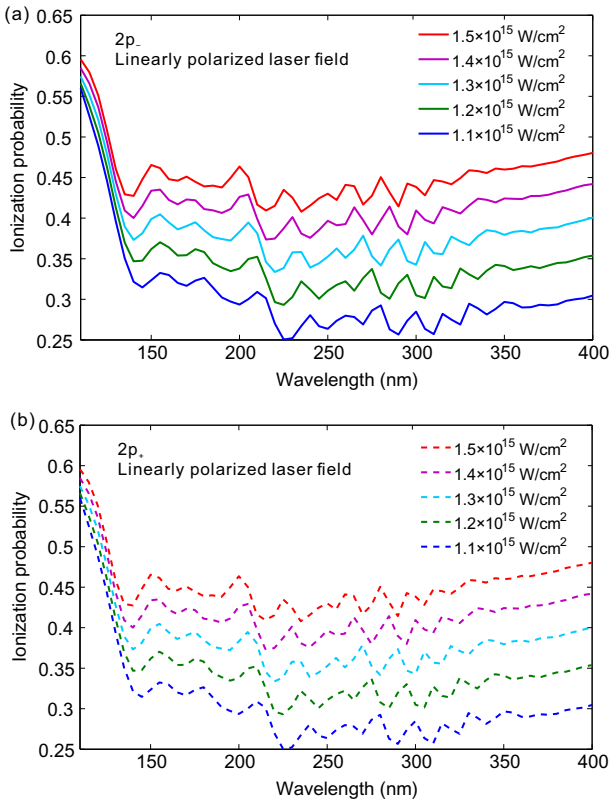

Fig. 4. Ionization probabilities for (a) $2p_-$ and (b) $2p_+$ orbitals driven by linearly polarized laser fields with laser intensities from $I = 1.1\times10^{15}$ W/cm^2 to 1.5×10^{15} W/cm^2 and laser wavelength varying from 110 nm to 400 nm. With linearly polarized laser fields, the curves of the ionization probabilities for $2p_-$ and $2p_+$ orbitals are the same for each laser intensity.

To uncover the process of the resonant enhancement driven by circularly polarized laser fields in detail, we study the time evolution of the occupations of the excited states. According to the requirement of the angular momentum conservation, when an electron with initial magnetic quantum number m_i absorbs ξ photons of the right or left circularly polarized laser pulse with photon spin of $+1$ or -1, the electron will be excited to the highly-lying state with final magnetic quantum number $m = m_i + \xi$ or $m_i - \xi$, respectively. Therefore, we should focus on transitions among states with different m. It can be easily done with our method of solving TDSE. For example, the results for the $2p_-$ orbital ($m_i = -1$), $I = 1.1\times10^{15}$ W/cm^2, and 150 nm are shown in Fig. 5. The laser field in Fig. 5(a) is right circularly polarized and in Fig. 5(b) left circularly polarized. The horizontal axis is m and vertical axis is time t. The color denotes the value of $\log_{10}[C(m,t)]$, where

$$C(m,t) = \sum_{\substack{k=1 \\ \eta_k^{(m)}<0}}^{N} \left|\langle\chi_k^{(m)}|\psi(t)\rangle\right|^2 \tag{22}$$

is the sum of modulus square of the projections of the wave function $\psi(t)$ onto field-free bound eigenstates $\chi_k^{(m)}$ for particular m.

In the counter-rotating case shown in Fig. 5(a), the $2p_-$ electron will be excited to states with

#257645 Received 20 Jan 2016; revised 15 Feb 2016; accepted 16 Feb 2016; published 19 Feb 2016

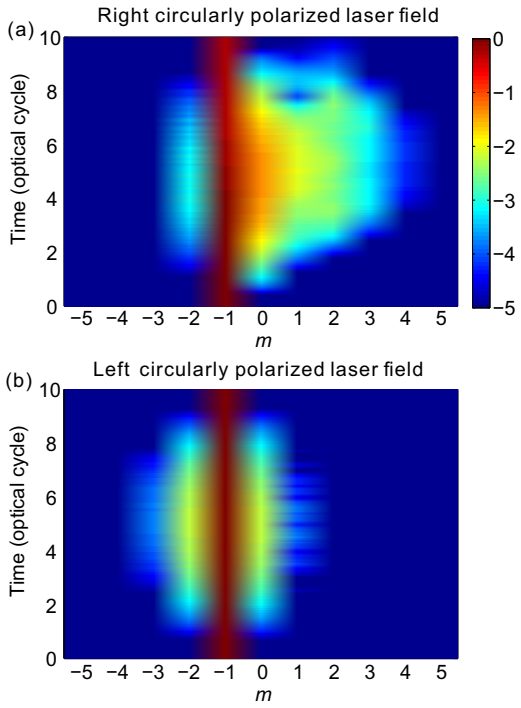

Fig. 5. Time evolution of the occupations of the bound states with different magnetic quantum numbers m starting from the $2p_-$ orbital driven by a (a) right or (b) left circularly polarized laser field with laser intensity $I = 1.1 \times 10^{15}$ W/cm^2 and laser wavelength 150 nm. The color denotes the value of $\log_{10}[C(m,t)]$, where $C(m,t)$ is the sum of modulus square of the projections of the wave function $\psi(t)$ onto field-free bound eigenstates $\chi_k^{(m)}$ for particular m.

magnetic quantum numbers $m = -1+\xi$ (ξ is positive and non-zero integer) in accord with the angular momentum conservation. The occupations are high for the first several states close to $m = -1$. In the co-rotating case shown in Fig. 5(b), the electron should be excited to state with $m = -1-\xi$. However, the occupations vanish very strongly even for $m \leq -3$. Comparing Figs. 5(a) and 5(b), it is shown that the $2p_-$ electron can easily absorb ξ photons of the right circularly polarized laser pulse and be excited to $m = -1+\xi$ states, but it is much more difficult to absorb ξ photons of the left circularly polarized laser pulse and jump to $m = -1-\xi$ states. In other words, the resonant excitation starting from $m = -1$ occurs much more easily in the positive direction ($|m|$ goes down to 0 and then increases towards $+\infty$) than in the negative direction ($|m|$ directly increases towards $+\infty$). This asymmetry of the transition probabilities between two different directions is just the reason for the helicity sensitivity of the resonant enhancement. Note that there are counter-intuitively non-zero occupations of states with $m = -2$ shown in Fig. 5(a) and $m = 0$ shown in Fig. 5(b). It seems conflicting with the angular momentum conservation and is due to the strongly modified wave functions by intense laser fields, where the calculated occupations in Fig. 5 are obtained by projecting the wave function $\psi(t)$ onto field-free eigenstates. However, this deviation does not change our discussion and conclusion.

To analyze the resonant enhancement, the energies of the first 10 lowest-lying eigenstates for $m = 0, \pm1, \pm2, \pm3, \pm4, \pm5$ are obtained by solving the eigenvalue equations and summarized

#257645 Received 20 Jan 2016; revised 15 Feb 2016; accepted 16 Feb 2016; published 19 Feb 2016

in Table I. Transitions among different states should follow the conservation of both energy and angular momentum. The conservation of energy requires that the transition to the highly-lying excited state happens when the absorbed photon energy $\xi\omega$ is equal to the energy gap between the initial and final states. The conservation of angular momentum requires that the change of m is equal to the number of absorbed photons ξ. As a result, if the electron is excited from the $m=-1$ state to the $m=-1\pm\xi$ state, the number of absorbed photons should be ξ and the absorbed energy should be $\xi\omega$.

Table 1. Energies of the first 10 lowest-lying eigenstates for $m=0$, ±1, ±2, ±3, ±4, ±5.

	$m=0$	$m=\pm1$	$m=\pm2$	$m=\pm3$	$m=\pm4$	$m=\pm5$
1	−2.9519	−0.7930	−0.0741	−0.0397	−0.0244	−0.0165
2	−0.2166	−0.1128	−0.0390	−0.0242	−0.0164	−0.0114
3	−0.0802	−0.0517	−0.0239	−0.0162	−0.0110	−0.0060
4	−0.0411	−0.0296	−0.0160	−0.0104	−0.0047	0.0013
5	−0.0249	−0.0191	−0.0099	−0.0033	0.0036	0.0106
6	−0.0165	−0.0127	−0.0022	0.0058	0.0138	0.0217
7	−0.0102	−0.0055	0.0076	0.0169	0.0258	0.0346
8	−0.0021	0.0038	0.0193	0.0298	0.0396	0.0492
9	0.0081	0.0152	0.0328	0.0445	0.0552	0.0656
10	0.0204	0.0285	0.0482	0.0609	0.0724	0.0837

Restricted by these two conservation laws, possible excitation channels and corresponding resonant laser wavelengths can be deduced. These wavelengths are shown in Fig. 6 with triangles and rectangles. The horizontally arranged triangles denote possible resonant wavelengths for the channels $m=-1\rightarrow-1+\xi$ (driven by right circularly polarized laser fields) and the horizontally arranged rectangles denote possible resonant wavelengths for the channels $m=-1\rightarrow-1-\xi$ (driven by left circularly polarized laser fields). The possible one-photon excitation channels $m=-1\rightarrow0$ and $m=-1\rightarrow-2$ are not shown because the corresponding resonant wavelengths are much shorter.

These resonant excitations will finally result in the helicity sensitive ionization enhancement. For example, the two-photon transitions $m=-1\rightarrow1$ lead to the first peak at about 120 nm as indicated by the first red arrow in Fig. 6. The second peak should be induced by the three-photon transitions $m=-1\rightarrow2$. The position of the peak is blue-shifted compared with the positions of corresponding resonant wavelengths, because the energy gaps between the initial and final states are enlarged due to the Stark shifts of highly-lying excited states with $m=2$ for such high laser intensity. Similarly, the third peak is induced by the four-photon transitions $m=-1\rightarrow4$, where the blue shift is much larger due to the larger Stark shifts of states with $m=3$. Figure 5(a) shows that the occupations are high for states with $m=1,2,3$ and the first three ionization peaks in Fig. 6 are most prominent. These two observations agree well. For ionization processes driven by left circularly polarized pulses, no ionization peaks are found in the ionization probability curve, because the transition probabilities to excited states with $m\leq-3$ are very small as already shown in Fig. 5(b).

4. Conclusion

In summary, strong-field ionization from $2p_{\pm}$ states in circularly polarized laser fields are investigated by solving 2D-TDSE in polar coordinates with the Lagrange mesh technique. The variation of the ionization probability as a function of the laser wavelength from the deep multiphoton regime to tunneling regime is discussed. In the deep multiphoton ionization regime,

#257645 Received 20 Jan 2016; revised 15 Feb 2016; accepted 16 Feb 2016; published 19 Feb 2016

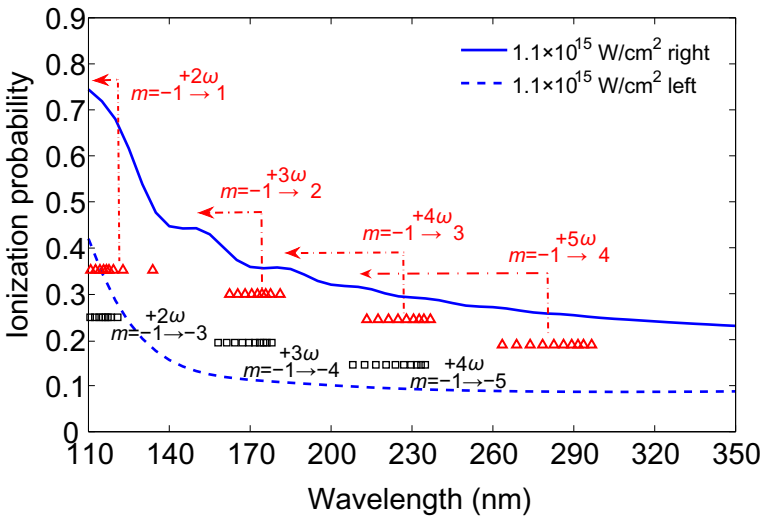

Fig. 6. Analysis of the origin of the ionization peaks. The blue curves present the ionization probabilities for the $2p_-$ orbital and for the laser intensity $I = 1.1 \times 10^{15}$ W/cm^2 of right (solid) and left (dashed) circularly polarized laser fields. The horizontally arranged red triangles denote the possible resonant wavelengths for the channels $m = -1 \to -1 + \xi$ (driven by right circularly polarized laser fields) and the horizontally arranged black rectangles denote the possible resonant wavelengths for the channels $m = -1 \to -1 - \xi$ (driven by left circularly polarized laser fields). Red arrows indicate the relationship between the ionization peaks and the excitation channels.

helicity sensitive ionization enhancement is observed. By analyzing the time-dependent evolution of the occupations of the excited bound states with different magnetic quantum numbers m, it is shown that this ionization enhancement is attributed to the multiphoton resonant transitions to excited states and the helicity sensitivity is due to the different transition probabilities for different excitation channels driven by left or right circularly polarized laser fields. This phenomenon shows the important role of excited states in the process of strong-field ionization from orbitals with internal angular momentum.

Acknowledgment

This work was supported by the National Natural Science Foundation of China under Grants No. 11234004, No. 11404123 and No. 61275126, the 973 Program of China under Grant No. 2011CB808103, and the Natural Science Foundation of Hubei Province under Grant No. 2014CFB174. Numerical simulations presented in this paper were carried out using the High Performance Computing Center experimental testbed in SCTS/CGCL (see http://grid.hust.edu.cn/hpcc).

#257645 Received 20 Jan 2016; revised 15 Feb 2016; accepted 16 Feb 2016; published 19 Feb 2016